MULTIFUNCTIONAL POLYBENZOXAZINE NANOSTRUCTURES FOR HYDROGEN STORAGE AND RELEASE AND THEIR DERIVED HETEROATOM-ENRICHED CARBON FOR SUPERCAPACITORS

INGITA TIWARI

DEPARTMENT OF MATERIALS SCIENCE AND ENGINEERING
INDIAN INSTITUTE OF TECHNOLOGY DELHI
JULY 2026

© **Indian Institute of Technology Delhi (IITD), New Delhi, 2026**

Multifunctional Polybenzoxazine Nanostructures for Hydrogen Storage and Release and Their Derived Heteroatom-Enriched Carbon for Supercapacitors

By

Ingita Tiwari

Department of Materials Science and Engineering

Submitted

in fulfilment of the requirements of the degree of Doctor of Philosophy

to the



Indian Institute of Technology Delhi

July 2026

*Dedicated to **my family***

CERTIFICATE

This is to certify that the thesis entitled "***Multifunctional Polybenzoxazine Nanostructures for Hydrogen Storage and Release and Their Derived Heteroatom-Enriched Carbon for Supercapacitors***" being submitted by *Ms. Ingita Tiwari* to the Indian Institute of Technology Delhi for the award of the degree of Doctor of Philosophy is a record of bonafide research work carried out by her. Ms. Ingita Tiwari has worked under my guidance and supervision and has fulfilled the requirements for the submission of her thesis, which, to our knowledge, has reached the requisite standard.

The results contained in this thesis are original and have not been submitted, in part or in full, to any University or Institute for the award of any degree or diploma.

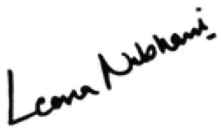

Dr. Leena Nebhani

Professor

Department of Materials Science and Engineering

Indian Institute of Technology Delhi

Hauz Khas, New Delhi, India-110016.

ACKNOWLEDGEMENTS

I would like to express my sincere gratitude to my supervisor, Prof. Leena Nebhani, whose mentorship has been fundamental to the completion of this doctoral work. Her constant guidance and insightful suggestions have greatly enriched this research, and her unwavering support at every stage of my PhD has significantly shaped my academic development and strengthened my confidence as an independent researcher. I am deeply indebted to her for the trust, academic freedom, and opportunities she provided throughout this journey.

I would also like to sincerely acknowledge my collaborators, Prof. Pravin Ingole and his students, Dr. Vaishali Tanwar, and Dr. Ajay from the Department of Chemistry, IIT Delhi, for their valuable cooperation and contributions, which significantly enriched the research. I further extend my gratitude to Prof. Cheng-Yu Wang from the Department of Materials Science and Engineering, National Yang Ming Chiao Tung University (NYCU), Taiwan, for his collaborative support and valuable inputs, which strengthened the interdisciplinary dimension of this work. I am also thankful to him for providing me with the opportunity for a short-term research stay in his PMEAL laboratory, which offered valuable international exposure and enriched my research experience. I also acknowledge Prof. Suryanarayana Vikrant Karra and Yash Mishra for their analytical inputs and constructive suggestions that enhanced the scientific depth.

I extend my sincere thanks to my SRC members, Prof. Josemon Jacob, Prof. Divya Nayar, and Prof. Sunil Kumar, for their valuable guidance, expertise, and constructive feedback, which significantly strengthened the quality and direction of this thesis.

I gratefully acknowledge the support and cooperation of my laboratory members: Dr. Pratibha Sharma, Dr. Aanchal Jaisingh, Dr. Tina Joshi, Dr. Amit Kumar, Dr. Lukkumanul Hakkim N., Dr. Nilanjan Mukherjee, Dr. Sonal Gupta, Dr. Harshal Mehta, Mr. Ehteshamul Islam, Gaurav Rai,

Priyanshi Goel, Kartik Gupta, Mr. Subhendu Sahoo, Mohd. Usman, Harshit Sachdeva, Shekhar, Vishnu Dutt, Siddhesh Rege, Abhishek Yadav, Thaseeb Rehman, Swapnil Mahajan, Rafiq Mohammad, Reshma K., Subhajit Bag, Premchand Nuthi, Hemant Gupta, Karishma, Chandan Nayak, Udhaya Kumar V., and Debjit Mal. The collaborative environment and professional interactions within the group have been invaluable to my academic growth.

I am equally thankful to the technical and administrative staff members of the Department of Materials Science and Engineering; Mr. Surender Sharma, Mr. Gajraj Singh, Mr. Gyanendra Yadav, Mr. Brijesh, Mr. Ashish Sharma, Mr. Jitendra Kumar, Ms. Shalini Arora, Mr. Amit Kumar, Mr. Jaswant, and Mr. Subhash Chand, for their consistent technical assistance and administrative support, which ensured the smooth conduct of my research work. The support from the Central Research Facility at IIT Delhi for advanced instrumentation is also gratefully acknowledged.

Finally, I express my heartfelt gratitude to my family for their unwavering support and encouragement. I am grateful to my father, Mr. Ajay Tiwari, for his guidance and constant motivation, which have been instrumental in all my achievements, and to my mother, Mrs. Indu Tiwari, for her faith and encouragement throughout this journey. I also recognize the support of my elder brother, Mr. Sudhanshu Tiwari. I would like to respectfully acknowledge my late grandfather, Prof. L. M. Tiwari, whose encouragement and belief in the value of higher education inspired me to pursue doctoral research. His guidance and vision continue to motivate me, and I dedicate this journey to his enduring legacy.

I sincerely thank everyone who supported and believed in me throughout this journey.

Ingita

(**INGITA TIWARI**)

ABSTRACT

The rational design of multifunctional materials capable of addressing challenges in energy storage and release remains a central objective in sustainable energy research. In this thesis, polybenzoxazines are explored as a versatile and molecularly flexible platform for the development of heteroatom-doped carbon materials for supercapacitors and functional polymer nanostructures for hydrogen storage and release. By integrating precursor molecular design, colloidal polymerization strategies, and nanoscale morphological control, this work establishes structure-property-function correlations for energy storage applications.

The controlled synthesis of multifunctional polybenzoxazine particles via a template-free dispersion polymerization approach combined with benzoxazine chemistry resulted in polybenzoxazine particles exhibiting high crosslinking density and enhanced char yield, enabling their transformation into nitrogen- and oxygen-codoped carbon particles through controlled carbonization. When evaluated as electrode materials in three-electrode and symmetric two-electrode configurations, these carbon particles exhibited enhanced specific capacitance and good rate capability, owing to the synergistic contributions of electric double-layer capacitance and pseudocapacitance arising from uniformly distributed functionalities within the carbon framework.

To further enhance electrochemical performance, hierarchical pore engineering was introduced using soft (1,3,5-trimethylbenzene) and hard (mesoporous silica) templating strategies. The templated polybenzoxazine particles enabled precise modulation of micro-, meso-, and macroporosity, resulting in hierarchically structured heteroatom-doped carbons with improved electrolyte accessibility and ion transport kinetics. The mesoporous silica-templated systems, in particular, demonstrated optimized pore distribution, resulting in further enhanced capacitance and improved rate performance compared to non-templated counterparts.

Beyond carbon-based supercapacitor application, this thesis demonstrates that polybenzoxazine particles can serve as chemically active nanoscaffolds for hydrogen storage and generation using complex hydrides. The incorporation of abundant functionalities in polybenzoxazine enabled strong interfacial interactions with ammonia borane through B–O and B–N interactions, destabilizing the dihydrogen bonding network and resulting in a reduced onset dehydrogenation temperature, a decreased activation energy, and the suppression of undesirable volatile by-products. Further, a nitrile-mediated self-assembly strategy was developed for catalytic sodium borohydride methanolysis. The nitrile-rich polybenzoxazine particles served as intrinsically active, metal-free heterogeneous catalysts for methanolysis, with improved hydrogen generation rates and lower activation energy than those of conventional supports.

This thesis demonstrates that polybenzoxazines represent a tailorable materials platform capable of functioning as (i) high-char-yield precursors for heteroatom-doped carbon electrodes, (ii) reactive nanoscaffolds for destabilizing chemical hydrides, and (iii) intrinsically active metal-free catalysts for hydrogen generation. By correlating molecular functionality, nanoscale morphology, and interfacial chemistry with electrochemical and catalytic performance, this work provides a rational design framework for functional polymer materials for energy storage and release applications.

सारांश

ऊर्जा भंडारण एवं ऊर्जा विमोचन से संबंधित चुनौतियों का समाधान करने में सक्षम बहु-कार्यात्मक सामग्रियों का तार्किक अभिकल्पन सतत ऊर्जा अनुसंधान का एक प्रमुख उद्देश्य है। इस शोध प्रबंध में **पॉलीबेंज़ॉक्साज़ीन** को सुपरकैपेसिटर हेतु हेटेरोएटम-डोप्ड कार्बन सामग्रियों तथा हाइड्रोजन भंडारण एवं विमोचन के लिए क्रियात्मक पॉलिमर नैनोसंरचनाओं के विकास हेतु एक बहुमुखी एवं आणविक स्तर पर नियंत्रित मंच के रूप में अन्वेषित किया गया है। प्रीकर्सर आणविक अभिकल्पन, कोलॉइडल पॉलिमरीकरण रणनीतियों तथा नैनोस्तरीय आकारिकी नियंत्रण के एकीकरण के माध्यम से इस कार्य में ऊर्जा भंडारण अनुप्रयोगों के लिए संरचना-गुण-कार्य संबंध स्थापित किए गए हैं।

टेम्पलेट-रहित डिस्पर्शन पॉलिमरीकरण विधि तथा बेंज़ॉक्साज़ीन रसायन विज्ञान के संयोजन से बहु-कार्यात्मक पॉलीबेंज़ॉक्साज़ीन कणों का नियंत्रित संश्लेषण किया गया। इन कणों में उच्च क्रॉसलिंक घनत्व एवं उन्नत चार उपज प्राप्त हुई, जिससे नियंत्रित कार्बनीकरण के माध्यम से इन्हें नाइट्रोजन एवं ऑक्सीजन सह-डोप्ड कार्बन कणों में रूपांतरित किया गया। तीन-इलेक्ट्रोड तथा सममित दो-इलेक्ट्रोड विन्यासों में इलेक्ट्रोड सामग्री के रूप में परीक्षण करने पर इन कार्बन कणों ने उच्च विशिष्ट धारिता एवं उत्तम रेट क्षमता प्रदर्शित की। यह प्रदर्शन कार्बन ढांचे में समान रूप से वितरित क्रियात्मक समूहों से उत्पन्न विद्युत द्वि-परत धारिता तथा स्यूडो-धारिता के सहक्रियात्मक योगदान के कारण संभव हुआ।

विद्युत-रासायनिक प्रदर्शन को और बेहतर बनाने हेतु सॉफ्ट (1,3,5-ट्राइमिथाइलबेंजीन) तथा हार्ड (मेसोपोरस सिलिका) टेम्पलेटिंग रणनीतियों द्वारा पदानुक्रमित छिद्र अभियांत्रिकी लागू की गई। टेम्पलेटेड पॉलीबेंज़ॉक्साज़ीन कणों ने माइक्रो-, मेसो- एवं मैक्रो-छिद्रता के सटीक नियंत्रण को संभव बनाया, जिससे पदानुक्रमित संरचना वाले हेटेरोएटम-डोप्ड कार्बन प्राप्त हुए जिनमें बेहतर इलेक्ट्रोलाइट पहुँच एवं आयन परिवहन गतिकी देखी गई। विशेष रूप से मेसोपोरस सिलिका-टेम्पलेटेड प्रणालियों में अनुकूलित छिद्र वितरण के कारण धारिता एवं रेट प्रदर्शन में अतिरिक्त वृद्धि हुई।

कार्बन प्रीकर्सर अनुप्रयोगों से आगे बढ़ते हुए, यह शोध दर्शाता है कि पॉलीबेंज़ॉक्साज़ीन कण जटिल हाइड्राइड्स के माध्यम से हाइड्रोजन भंडारण एवं उत्पादन के लिए रासायनिक रूप से सक्रिय नैनो-स्कैफोल्ड के रूप में भी कार्य कर सकते हैं। प्रचुर क्रियात्मक समूहों की उपस्थिति के कारण अमोनिया बोरेन के साथ B-O एवं B-N अंतःक्रियाएँ सशक्त हुईं, जिससे डाइहाइड्रोजन बंधन नेटवर्क का अस्थिरीकरण हुआ तथा डिहाइड्रोजनीकरण का आरंभिक तापमान एवं सक्रियण ऊर्जा कम हुई, साथ ही अवांछित वाष्पशील उप-उत्पादों का दमन हुआ। इसके अतिरिक्त, सोडियम बोरोहाइड्राइड मिथेनोलाइसिस के लिए नाइट्राइल-प्रेरित स्व-संयोजन रणनीति विकसित की गई, जिसमें नाइट्राइल-समृद्ध PBz कण आंतरिक रूप से सक्रिय, धातु-रहित विषम उत्प्रेरक के रूप में कार्य करते हुए पारंपरिक पॉलिमर सपोर्ट की तुलना में अधिक हाइड्रोजन उत्पादन दर एवं कम सक्रियण ऊर्जा प्रदर्शित करते हैं।

यह शोध सिद्ध करता है कि पॉलीबेंज़ॉक्साज़ीन एक एकीकृत सामग्री मंच का प्रतिनिधित्व करते हैं, जो (i) उच्च चार उपज वाले हेटेरोएटम-डोप्ड कार्बन इलेक्ट्रोड के प्रीकर्सर, (ii) रासायनिक हाइड्राइड्स के अस्थिरीकरण हेतु सक्रिय नैनो-स्कैफोल्ड, तथा (iii) हाइड्रोजन उत्पादन के लिए आंतरिक रूप से सक्रिय धातु-रहित उत्प्रेरक के रूप में कार्य कर सकते हैं। आणविक क्रियात्मकता, नैनोस्तरीय आकारिकी तथा अंतरफलक रसायन को विद्युत-रासायनिक एवं उत्प्रेरक प्रदर्शन से संबद्ध करते हुए यह कार्य ऊर्जा भंडारण एवं विमोचन अनुप्रयोगों हेतु क्रियात्मक पॉलिमर सामग्रियों के तार्किक अभिकल्पन के लिए एक रूपरेखा प्रदान करता है।

TABLE OF CONTENTS

CERTIFICATE ..... **i**
ACKNOWLEDGEMENTS ..... **ii**
ABSTRACT ..... **iv**
LIST OF FIGURES ..... **xii**
LIST OF TABLES ..... **xxii**
LIST OF ABBREVIATIONS ..... **xxiv**
LIST OF SYMBOLS ..... **xxvii**
Chapter 1. Introduction and Literature Review **1**
1. Introduction **2**
1.1. Polybenzoxazine 2
1.2. Polybenzoxazine-Based Particles 5
1.2.1. Zero-dimensional Polybenzoxazine Particles 6
1.2.2. One-dimensional Polybenzoxazine Structures 9
1.2.3. Two-dimensional Polybenzoxazine Structures 11
1.2.4 Three-dimensional Polybenzoxazine Structures 14
1.2.4.1. Spheres 14
1.2.4.2. Foams 17
1.2.4.3. Monoliths 20
1.2.4.4 Aerogels 22
1.3. Solid-State Hydrogen Storage and Release 33
1.3.1. Functional structures for enhanced hydrogen storage and release by thermolysis 34
1.3.2. Functional structures for enhanced hydrogen storage and release by methanolysis 40
1.4. PBz Derived Heteroatom-Enriched Carbon 44
1.4.1. Deriving Carbon Materials From Polybenzoxazines Via Carbonization 48
1.4.1.1. Influence of Carbonization Temperature 49
1.4.1.2. Influence of Precursors 52
1.4.1.3. Influence of Activation Conditions 55

1.5. Polybenzoxazine-derived Carbon for Supercapacitors 58
1.6. Gap in Literature and Objective of Work 65
1.7. Thesis format 67
1.8. References 71
Chapter 2. Heteroatom-Enriched Carbon Particles Derived From Multifunctional Polybenzoxazine Particles For High-Performance Supercapacitors 89
2.1. Introduction 90
2.2. Experimental 94
2.2.1. Materials 94
2.2.2. Experimental Method 94
2.2.3. Characterization Techniques 95
2.2.4. Electrode Fabrication and Electrochemical Measurement 98
2.3. Results and Discussion 101
2.3.1. Synthesis and Morphology Control of Polymer Nanospheres 101
2.3.1.1. Influence of Stoichiometry Ratio on Particle Morphology 103
2.3.1.2. Influence of Solvent Ratio on Particle Morphology 108
2.3.1.3. Influence of Precursor Concentration on Particle Formation 110
2.3.2. Mechanism of Polymer Particle Formation 111
2.3.3. Controlled Carbonization to Attain Heteroatom-Doped Porous Carbon 113
2.3.4. Evaluation of Polybenzoxazine-Derived Heteroatom-Doped Carbon Particles For Supercapacitance Application 123
2.3.4.1. Electrochemical Performance in a Three-Electrode System 123
2.3.4.2. Electrochemical Performance in Symmetric (C-P-PEI//C-P-PEI) and Asymmetric (C-P-PEI//AC) Devices 130
2.4. Conclusions 138
2.5. References 139
Chapter 3. Nanostructured Polybenzoxazine Particles-Supported Ammonia Borane for Hydrogen Storage and Release 146
3.1. Introduction 147
3.2. Experimental 150
3.2.1. Materials 150
3.2.2. Experimental Method 150

3.2.2.1. Synthesis of Aniline-Derived Polybenzoxazine Particles (PA) 150
3.2.2.2. Synthesis of 4-Aminobenzonitrile-Derived Polybenzoxazine Particles (PAB) . 151
3.2.2.3. Synthesis of PA/PAB in the Presence of 1,3,5-Trimethylbenzene (PA-M/PAB-M) 151
3.2.2.4. Synthesis of PA/PAB in the Presence of Mesoporous Silica (PA-MS/PAB-MS) 151
3.2.2.5 Synthesis of AB@PA and AB@PAB 152
3.2.3. Characterization Techniques 153
3.3. Results and Discussion 155
3.3.1. Polybenzoxazine Particle Synthesis 155
3.3.2 Hydrogen Storage Performance 168
3.3.3. Mechanism of Polybenzoxazine-Supported AB Dehydrogenation 183
3.4. Conclusion 189
3.5. References 190
Chapter 4. Engineered Polybenzoxazine Particles via Mesoporous Silica Templating Towards Hierarchical Heteroatom-Doped Carbon Nanostructures for High-Rate Capbility Supercapacitors 197
4.1. Introduction 198
4.2. Experimental 201
4.2.1. Materials 201
4.2.2. Experimental Method 201
4.2.2.1. Synthesis of Aniline and 4-Aminobenzonitrile-Derived Polybenzoxazine Particles 201
4.2.2.2. Synthesis of 1,3,5-Trimethylbenzene-assisted PA/PAB (PA-M/PAB-M) 202
4.2.2.3. Synthesis of Mesoporous Silica-assisted PA/PAB (PA-MS/PAB-MS) 202
4.2.2.4. Carbonization For Heteroatom-Doped Carbon 203
4.3. Characterization Techniques 204
4.4. Electrode Preparation and Electrochemical Characterization 204
4.5. Results and Discussions 206
4.5.1. Effect of Precursor Stoichiometry on Particle Morphology and Crosslinking Behavior 207
4.5.2. Effect of Amine on Particle Morphology and Network Formation 210

4.5.3. Effect of templates on morphology and textural characteristics 211
4.5.4. Controlled Carbonization to Attain Heteroatom-Doped Porous Carbon 216
4.5.5. Electrochemical Measurements 221
4.5.5.1. Electrochemical Evaluation in Three-Electrode Configuration 221
4.5.5.2. Electrochemical Evaluation in Two-electrode Configuration 230
4.6. Conclusion 233
4.7. References 234
Chapter 5. Tuning Polybenzoxazine Particle Morphology through Nitrile Functionality for Enhanced Catalytic Sodium Borohydride Methanolysis 237
5.1. Introduction 238
5.2. Experimental 242
5.2.1. Materials 242
5.2.2. Experimental Method 242
5.2.2.1. Synthesis of 4-Aminophthalonitrile-Derived Polybenzoxazine Particles 242
5.2.2.2. Catalytic Methanolysis of Sodium Borohydride 244
5.3. Characterization Techniques 245
5.4. Results and Discussions 245
5.4.1. Influence of Stoichiometric Ratio on Particle Morphology 247
5.4.2. Influence of Solvent Ratio on Morphology 249
5.4.3. Influence of Precursor Concentration 250
5.4.4. 4-Aminobenzonitrile-derived Polybenzoxazine as the Control Sample 251
5.4.5. Catalytic Methanolysis of Sodium Borohydride using PAP 256
5.5. Conclusions 269
5.6. References 269
Chapter 6. Conclusion and Future Outlook 274
BIODATA 278

LIST OF FIGURES

Chapter 1

Figure 1.1. Timeline of significant milestones in the evolution of polybenzoxazine from phenolic resins. 2

Figure 1.2. (A) Reaction scheme for benzoxazine monomer synthesis via (i) Mannich like condensation of phenol, amine, and paraformaldehyde, (ii) 1-(bromomethyl)-2-(chloromethoxy) benzene, (iii) Dehydration of N-(2-hydroxybenzyl)-3-aminopropanoic; (B) (i)-(ii) Various mechanisms proposed for the ring opening polymerization of benzoxazines. 5

Figure 1.3. (A) Scheme and SEM micrographs of polybenzoxazine nanospheres; and (B) SEM micrographs of the polymer nanospheres synthesized at different initial reaction temperatures. .. 8

Figure 1.4. (A),(B) Synthesis of PBz nanofibers by electrospinning and in situ polymerization; and (C) FESEM images of hybrid PVBNF and the corresponding cured nanofibers PBZNF..... 10

Figure 1.5. (A) Synthesis of hybrid polybenzoxazine nanosheets; (B) Formation mechanism via dual-templating strategy; (C) Thermoregulated phase transition for the formation of thin polymer nanoplates; and (D) FTIR and Zeta potential of dual-templated system before and after DAH functionalization 12

Figure 1.6. Schematic representation for (A) coral-like carbon formation; and (B) Dual-templated system with different morphologies..... 15

Figure 1.7. (A) Partially cured polybenzoxazine and polybenzoxazine foam at foaming temperature (T_f) = 220 °C; (B) SEM micrographs; and (C) Cell size distribution at different foaming temperatures..... 19

Figure 1.8. (A) Photograph and SEM image of polymer; and (B) Synthesis scheme of Poly(benzoxazine-co-resol)-Based Monoliths..... 21

Figure 1.9. (A) SEM images of PBz aerogels at different sol concentrations (xx); (B) Schematic illustration of novel polybenzoxazine/GO nanocomposite aerogels; and (C) SEM and TEM images of TBOZ monomer-derived PBz aerogel..... 26

Figure 1.10. (A) Catalytic mechanism for the re/dehydrogenation of $NaAlH_4$ with Ti_3C_2/NC composite; (B) Synthesis procedure of MBH@ANPC; (C) Catalytic mechanism of NiCo NPs in H_2 desorption from $NaBH_4$@NiCo-NC; (D) Schematic correlation between the carbon structure,

nanoconfinement, and dehydrogenation performance; (E) Dehydrogenation kinetics; and (F) Rehydrogenation kinetics of pure MgH_2, MgH_2-Gr and MgH_2-VS_2..... 36
Figure 1.11. (A) Influence of triazole-based organocatalysts on HGR; (B) Schematic representation of PEI microgels protonation; (C) Synthesis of NiB/HAP catalyst using wet-impregnation method; and (D) Proposed mechanism of interaction of Hf-MEL with $NaBH_4$. ... 43
Figure 1.12. Thermal decomposition products at different stages of bisphenol-A, aniline, and formaldehyde-based PBz 49
Figure 1.13. (A) Synthesis of nitrogen-doped microporous carbon from fully bio-derived benzoxazine monomer using vanillin, furfurylamine, and paraformaldehyde; (B) SEM images and nitrogen adsorption isotherms of the carbon spheres derived at 500 °C, 800 °C and 900 °C; (C) SEM and TEM images of hierarchical carbon monoliths with hexagonal mesopore array; and (D) Comparative photographs of phenolic (RF) and polybenzoxazine (PBO) aerogels before and after carbonization..... 52
Figure 1.14. (A) Cyclic Voltammogram, Galvanostatic charge/discharge curve, Specific capacitances, and Cyclability of the carbon sample; and (B) Electrochemical performance of BNPC-0.15..... 63

Chapter 2

Figure 2.1. Schematic illustration of the N, O-codoped carbon particles derived from polybenzoxazine colloidal spheres via template-free extended sol-gel method. 102
Figure 2.2. FESEM micrographs of polybenzoxazine particles in ethanol/water (volume ratio 1/3) reaction medium with varying stoichiometric ratio (A) P-PEI_2:1:12, (B) P-PEI_3:1:18, (C) P-PEI_5:1:30, (D) P-PEI_7:1:40, (E) P-PEI_9:1:54, (F) P-PEI_10:1:60, and (G) P-PEI_12:1:72. 103
Figure 2.3. Particle size distribution bar graph of polybenzoxazine particles with phloroglucinol: PEI: formaldehyde stoichiometric ratio of (A) 7:1:40, (B) 9:1:54, and (C) 10:1:60. 104
Figure 2.4. (A) Solid-state ^{13}C CP/MAS NMR spectrum of polybenzoxazine particles with the plausible structure, (B) FTIR spectra, (C) Non-isothermal DSC profiles, (D) TGA profile in the range of 30 to 800 °C, and (E) Derivative Thermogravimetry profiles of polybenzoxazine particles for systems with phloroglucinol: amine: formaldehyde ratios of 7:1:40, 9:1:54, 10:1:60, and 12:1:72. 105

Figure 2.5. FESEM images of P-PEI_9:1:54 system attained at low initial reaction temperature of 0 °C. 107
Figure 2.6. FESEM micrographs of P-PEI_9:1:54 system with ethanol/water volume ratio of (A) 0/320, (B) 40/280, (C) 80/240, (D) 120/200, (E) 200/120, (F) 240/80, (G) 280/40, and (H) 320/0. 109
Figure 2.7. Particle size distribution bar graph of P-PEI_9:1:54 system with ethanol/water ratio of (a) 0/320, (b) 40/280, (c) 80/240, (d) 120/200, (e) 200/120, (f) 240/80, (g) 280/40, and (h) 320/0. 109
Figure 2.8. FESEM images of P-PEI_9:1:54 system with overall precursor concentration of (A) 60 mmol/L, (B) 120 mmol/L, and (C) 240 mmol/L. 110
Figure 2.9. Synthesis scheme for the preparation of heteroatom-doped carbon structure using phloroglucinol, PEI, and formaldehyde with plausible structure of polymer and carbon. 113
Figure 2.10. FESEM images of polybenzoxazine particles thermally treated at (A) 150 °C, (B) 200 °C, (C) 300 °C, (D) 400 °C, and (E) 500 °C.....114
Figure 2.11. (A) Elemental mapping, and (B) elemental composition obtained from EDX spectrum of polybenzoxazine particles P-PEI_9:1 thermally treated at 400 °C.....114
Figure 2.12. (A) Elemental mapping, and (B) elemental composition obtained from EDX spectrum of polybenzoxazine particles P-PEI_9:1 thermally treated at 500 °C.....115
Figure 2.13. Raman spectra of polybenzoxazine particles thermally treated at (A) 150 °C, (B) 200 °C, (C) 300 °C, and (D) 400 °C. 116
Figure 2.14. FESEM images of P-PEI_9:1:54 polybenzoxazine particles post-cured at (A) 100 °C, and (B) 150 °C for 8 h under an air atmosphere. 116
Figure 2.15. Solid-state ^{13}C CP/MAS NMR spectrum of polybenzoxazine particles post-cured at 150 °C for 8 h with the plausible structure. 117
Figure 2.16. FESEM images of (A) polybenzoxazine particles **(P-PEI_9:1:54)**; (B) heteroatom-doped carbon spheres obtained by direct carbonization at 400 °C for 8 h under argon atmosphere; (C) polybenzoxazine particles post-cured at 150 °C for 8 h **(P-PEI@150)**; (D) heteroatom-doped carbon spheres obtained by subjecting the post-cured sample to carbonization at 400 °C for 8 h under argon atmosphere **(C-P-PEI)**; and (E) TEM image of doped carbon sphere, where the inset shows the detailed morphology at a higher magnification. 118

Figure 2.17. (A) Raman spectra of C-PPEI, (B) XRD pattern for polybenzoxazine-derived heteroatom-doped carbon **(C-P-PEI),** and (C) BET isotherms for polybenzoxazine precursor heteroatom-doped carbon particles **(C-P-PEI)**.....119
Figure 2.18. Elemental mapping, and elemental composition obtained from EDX spectrum for (A) P-PEI_9:1:54; (B) P-PEI_9:1:54-SC, and (C) C-P-PEI..... 121
Figure 2.19. (A) Wide XPS spectra recorded for P-PEI_9:1 polybenzoxazine particles, step-cured P-PEI_9:1:54, and carbonized P-PEI_9:1:54; Narrow XPS scans recorded for (B) carbon; (C) nitrogen; and (D) oxygen in C-P-PEI. 122
Figure 2.20. Electrochemical performance of the heteroatom-doped carbon C-P-PEI_9:1:54 in different electrolytes. 124
Figure 2.21. Electrochemical performance evaluation of C-P-PEI in a three-electrode system using: CV curves (A) at different potential windows, (B) at varying scan rates in an optimized potential window, (C) GCD curves measured at varying current densities, (D) C_{sp} values measured at different current densities, (E) Pseudocapacitance and EDLC contribution in the total C_{sp} value measured at 10 A/g, (F) Ragone plot of P_d Vs E_d, (G) Nyquist plot; and (H) Bode phase angle plot in the frequency range of 1 to 10^4 Hz. 127
Figure 2.22. (A) CV, and (B) GCD at different mass loading in three-electrode configuration.127
Figure 2.23. Plausible redox reactions involving different nitrogen species along with quinone oxygen species in acidic medium. 128
Figure 2.24. GCD curve measured at 3 A/g and 10 A/g for three-electrode system..... 129
Figure 2.25. Electrochemical performance evaluation in C-P-PEI//C-P-PEI device using: CV curves (A) measured at different potential windows, (B) at varying scan rates; GCD curves (C) measured in different potential windows, (D) at varying current densities, (E) C_s values measured at different current densities, and (F) Ragone plot of (P_d) Vs (E_d), (G) Nyquist plot, where the inset figure shows the Warburg region in the midfrequency range; and (H) stability retention after 5000 cycles..... 132
Figure 2.26. (A) CV and (B) GCD for three-electrode and two-electrode system. 134
Figure 2.27. Raman spectra of C-P-PEI-based electrode before and after being subjected to 5000 charge-discharge cycles. 135
Figure 2.28. (A) Nyquist plot; and (B) Bode phase angle plot before and after subjecting to cyclic stability tests in the two-electrode configuration. 135

Figure 2.29. Electrochemical performance of C-P-PEI//AC device, (A) Comparative CV curves for C-P-PEI and AC, CV at (B) varying potential windows, (C) at varying scan rates (10 - 100 mV s^{-1}), (D) GCD curves at varying current densities, (E) C_{sp} vs current density, and (F) C_{sp} retention up to 2500 cycles where the inset shows Nyquist plot before and after the cyclic stability test. 136
Figure 2.30. Comparative values of supercapacitor performance of C-P-PEI with literature reports of other polybenzoxazine-derived carbon materials obtained using several precursors including, nitrile-modified vanillin and 2-thiophenemethylamine,[60] guaiacol and PEI,[61] melamine and eugenol,[62] hydroquinone and phenylethylamine,[63] apigenin and furfurylamine,[64] phenol and aniline,[65] phenol and ethylenediamine,[66] phenol and thiourea,[67] 1,1,1-tris(4-hydroxyphenyl)ethane and 1,3,5- triphenylhexahydro-1,3,5-triazine,[68] 4-cyanophenol and urea,[69] in three-electrode system. 138

Chapter 3

Scheme 3.1. Schematic representation of colloidal polybenzoxazine formation from phloroglucinol, formaldehyde, and (A) aniline or (B) 4-aminobenzonitrile with polymer network evolution over reaction time. 156
Figure 3.1. FESEM micrograph of (A) PAB at phloroglucinol: 4-aminobenzonitrile: formaldehyde molar ratio of 1:3:6; (B) PA at phloroglucinol: aniline: formaldehyde molar ratio of 1:3:6; (C) PA at phloroglucinol: aniline: formaldehyde molar ratio of 1:4:8; (D) Solid-state ^{13}C CP/MAS NMR spectrum of PAB; and (E) Solid-state ^{13}C CP/MAS NMR spectrum of PA. 158
Figure 3.2. FESEM micrographs of (A) PAB step-cured at 220 °C; (B) PA step-cured at 150 °C; (C) FTIR spectra of step-cured PAB and PA; (D) non-isothermal DSC profile of PAB and PA; (E) TGA, and (F) DTG profiles of PAB and PA in the temperature range of 30 to 800 °C. 161
Figure 3.3. FESEM micrographs of (A) PAB; (B) PA; (C) PAB-M synthesized in the presence of 1,3,5-trimethylbenzene; (D) PA-M synthesized in the presence of 1,3,5-trimethylbenzene; (E) PAB-MS synthesized in the presence of MS; (F) PA-MS synthesized in the presence of MS; (G) N_2 adsorption-desorption isotherms of PA, PA-M, and PA-MS, and (H) N_2 adsorption-desorption isotherms of PAB, PAB-M, and PAB-MS..... 163
Figure 3.4. Time-resolved FESEM images of PA-M at (A) t_0 at RT; (B) t_{10} at RT; (C) t_{20} at RT; (D) t_{30} at RT; (E) t_{60} at RT; and (F) t_{90} at 80 °C. 164

Figure 3.5. Schematic representation of the synthesis of polybenzoxazine particles using (A) TMB as a swelling agent in 4-aminobenzonitrile system; (B) TMB as a soft porogen in aniline system; and (C) MS as a hard template, highlighting the influence of templating strategy on polymer assembly and pore architecture. 165
Figure 3.6. (A) FESEM micrograph of synthesized mesoporous silica and (B) BET isotherms for mesoporous silica, where the inset shows the pore-size distribution measured using BJH model. 166
Figure 3.7. Pore size distribution using BJH model for (A) PAB-MS and (B) PA-MS. 167
Figure 3.8. FTIR spectra of neat AB compared with (A) PAB and AB@PAB; and (B) PA and AB@PA..... 168
Figure 3.9. Comparative hydrogen release profile for (A) neat AB, AB@PA, AB@PA-M, and AB@PA-MS; (B) neat AB, AB@PAB, AB@PAB-M, and AB@PAB-MS; Dehydrogenation kinetics of (C) AB@PAB-M at 80 °C, 90 °C, 100 °C, and 120 °C; (D) AB@PA-M at 80 °C, 90 °C, 100 °C, and 120 °C; (E) neat AB at 90 °C, 100 °C, and 120 °C; and (F) Activation energies using Arrhenius plot for AB@PAB-M and AB@PA-M. 169
Figure 3.10. Ammonia TPD-MS profiles of neat AB compared with (A) template-free PAB and PA system; (B) PAB-M and PA-M particles; and (C) PAB-MS and PA-MS system. 170
Figure 3.11. Hydrogen release profiles of (A) PAB, PAB-M, and PAB-MS; and (B) PA, PA-M, and PA-MS. 171
Figure 3.12. Comparative hydrogen release profiles of (A) AB@PAB-M and AB@PAB-M_mixed; and (B) AB@PA-M and AB@PA-M_mixed. 172
Figure 3.13. TPD-MS profile of standard TiH_2 at (A) 50 mg; (B) 100 mg; (C) 150 mg; and (D) Hydrogen release quantification by peak area calibration. 173
Figure 3.14. H_2 release quantification in AB. 174
Figure 3.15. XPS survey spectra (A) AB@PA-M and (B) AB@PAB-M; High-resolution B1s spectra of (C) AB@PA-M and (D) AB@PAB-M. 176
Figure 3.16. Schematic illustration of ammonia borane (AB) interaction with polybenzoxazine particles synthesized in the presence of TMB using (A) 4-aminobenzonitrile; and (B) aniline. 179
Figure 3.17. XRD profile of (A) PA-M; (B) PAB-M; ^{11}B Solid-state NMR spectra of (C) AB@PA-M, (D) AB@PAB-M, and XRD profile of (E) PA-MS; (F) PAB-MS after dehydrogenation cycle. 180

Figure 3.18. High-resolution B1s spectra of (A) AB@PAB-M and (B) de-AB@PAB-M; N1s spectra of (C) AB@PAB-M and (D) de-AB@PAB-M. 181
Figure 3.19. (A) Plausible interactions between the surface functionalities of polybenzoxazine particles with AB; (B,C) Interaction of AB with hydroxyl groups present in both PA and PAB; and (D,E) Interaction of AB with nitrile groups present in PAB. 187
Figure 3.20. TPD-MS profiles of (A) PA-M and (B) PAB-M post three regeneration-dehydrogenation cycles. 188
Figure 3.21. Elemental distribution of (A) PAB-M; (B) PAB-M-3-de; (C) PA-M; (D) PA-M-3-de; comparative FTIR spectra of (E) PA-M and PA-M-3-de; and (F) PAB-M and PAB-M-3-de. ... 189

Chapter 4

Scheme 4.1. Synthesis scheme for polybenzoxazine derived from (A) phloroglucinol, 4-aminobenzonitrile, and formaldehyde, and (B) phloroglucinol, aniline, and formaldehyde. 207
Figure 4.1. FESEM micrographs of polybenzoxazine particles in ethanol/water (volume ratio 1/4) reaction medium with varying stoichiometric ratio (A) PAB_1:2:4, (B) PAB_1:3:6, (C) PAB_1:4:8, (D) PAB_1:5:10, (E) PA_1:2:4, (F) PA_1:3:6, (G) PA_1:4:8, and (H) PA_1:5:10 209
Figure 4.2. (A) TGA profile of PAB in the range of 30 to 800 °C, (B) DTG profile of PAB, (C) TGA profile of PA in the range of 30 to 800 °C, and (D) DTG profile of PA with phloroglucinol: amine: formaldehyde ratios of 1:2:4, 1:3:6, 1:4:8, and 1:5:10 210
Figure 4.3. FESEM images showing the effect of 1,3,5-trimethylbenzene incorporation at (A) 1.5 v/v%; (B) 2.5 v/v%, (C) 3.5 v/v% in PAB; and (D) 1.5 v/v%; (E) 2.5 v/v%, (F) 3.5 v/v% in PA. 212
Figure 4.4. FESEM images illustrating the effect of MS incorporation at (A) 7.5 w/w%; (B) 10 w/w%, (C) 15 w/w%, (D) 25 w/w% in PAB system; and (E) 7.5 w/w%; (F) 10 w/w%, (G) 15 w/w%, (H) 25 w/w% in PA system. 213
Figure 4.5. N_2 adsorption-desorption isotherms of (A) PA, PA-M, and MS/PA, and (B) PAB, PAB-M, and MS/PAB. 215
Figure 4.6. FESEM images of (A) C-PAB; (B) C-PAB-M; (C) C-PAB-MS, and (D) C-PA; (E) C-PA-M; and (F) C-PA-MS. 216

Figure 4.7. Comparative XRD pattern (A) C-PA and C-PAB; (C) C-PA-M and C-PAB-M; (E) C-PA-MS and C-PAB-MS; and comparative Raman spectra of (B) C-PA and C-PAB; (D) C-PA-M and C-PAB-M; (F) C-PA-MS and C-PAB-MS. 218
Figure 4.8. N_2 adsorption-desorption isotherms of (A) C-PAB, C-PAB-M, and C-PAB-MS, and (B) C-PA, C-PA-M, and C-PA-MS, Pore size distribution using BJH model for (C) PAB and (D) PA system. 219
Figure 4.9. Comparative CV of (A) C-PAB, C-PAB-M, and C-PAB-MS; (B) C-PA, C-PA-M, and C-PA-MS at scan rate of 25 mV s^{-1}; GCD curves of (C) C-PAB, C-PAB-M, and C-PAB-MS; (D) C-PA, C-PA-M, and C-PA-MS; C_{sp} values measured at 10 A/g for (E) C-PAB, C-PAB-M, and C-PAB-MS; and (F) C-PA, C-PA-M, and C-PA-MS. 223
Figure 4.10. (A) Wide XPS spectra recorded for C-PA-MS; Narrow XPS scans recorded for (B) carbon, (C) nitrogen, and (D) oxygen in C-PA-MS. 225
Figure 4.11. Electrochemical performance of C-PA-MS in (A) different electrolytes measured in a three-electrode system, (B) at different potential windows at a constant scan rate of 25 mV s^{-1}, (C) at varying scan rates in an optimized potential window of 0 to 0.8 V, (D) GCD curves measured at varying current densities, (E) C_{sp} values measured at different current densities, and (F) CV profile of as-synthesized MS. 226
Figure 4.12. (A) Logarithmic relationship between peak current (I) and scan rate (ν), (B) b-values at different potentials, (C) Linear fit of $i/\nu^{0.5}$ versus $\nu^{0.5}$, (D) Quantitative estimation of capacitive and diffusion-controlled contributions at varying scan rates; (E) Capacitance distribution at 25 mV s^{-1} 228
Figure 4.13. (A) Nyquist plot of the electrochemical impedance spectrum with equivalent-circuit fitting (inset) for the electrode; and (B) Bode phase-angle plot. 229
Figure 4.14. Electrochemical performance evaluation in C-PA-MS//C-PA-MS symmetric device using: (A) CV curves measured at different potential windows, (B) at varying scan rates; GCD curves (C) at varying current densities, (D) Ragone plot of (P_d) Vs (E_d), and (E) C_{sp} values measured at different current densities. 231
Figure 4.15. Electrochemical performance of C-PA-MS//AC asymmetric device, (A) CV at varying scan rates (5-200 mV s^{-1}), (B) GCD curves at varying current densities, and (C) C_{sp} vs current density. 232

Chapter 5

Scheme 5.1. Schematic illustration showing formation of needle-shaped PAP particles. 247
Figure 5.1. FESEM micrographs of polybenzoxazine particles in ethanol/water (volume ratio 1/3) reaction medium with varying stoichiometric ratio (A) PAP_1:1:2, (B) PAP_1:2:4, (C) PAP_1:3:6, (D) PAP_1:4:8, (E) PAP_1:6:12, (F) PAP_1:8:16, and (G) TGA profiles in the range 30 to 800 °C. 248
Figure 5.2. FESEM micrographs of PAP_1:2:4 system with ethanol/water volume ratio of (A) 240/80, (B) 160/160, (C) 80/240, and (D) 10/310. 249
Figure 5.3. FESEM images of PAP_1:2:4 system with overall precursor concentration of (A) 30 mmol/L, (B) 70 mmol/L, and (C) 150 mmol/L. 250
Figure 5.4. Schematic representation of morphology evolution in PAB particles under different synthesis conditions. 252
Figure 5.5. (A) ^{13}C Solid-state NMR of PAP_1:2:4, (B) FTIR of PAP_1:2:4, (C) DSC of PAP_1:2:4 and PAP_1:2:4-SC, and (D) BET isotherm for PAP_1:2:4-SC. 253
Figure 5.6. FESEM micrographs for post-cured PAP_1:2:4..... 255
Figure 5.7. Comparative XRD profiles of PAP and PAB..... 256
Figure 5.8. Comparative FTIR spectra of sodium borohydride (NB) in presence of (A) PPEI, (B) PA, (C) PAB, and (D) PAP. 257
Figure 5.9. Polybenzoxazine structures of (A) PPEI, (B) PA, (C) PAB, and (D) PAP, (E) Comparative catalytic performance for hydrogen generation, and (F) HGR and $n(H_2)/n(NB)$ of the catalytic systems. 258
Figure 5.10. Temperature-dependent performance of (A) PPEI, (C) PA, (E) PAB, (G) PAP and the (B, D, F, H) corresponding HGR values. 260
Figure 5.11. Activation energies using Arrhenius plots for (A) PPEI, (B) PA, (C) PAB, (D) PAP, and (E) comparative E_a values. 261
Figure 5.12. Schematic representation of plausible interactions of catalytic PAP particles with sodium borohydride and methanol..... 263
Figure 5.13. Effect of (A) catalyst amount, (C) $NaBH_4$ amount, (E) methanol content on hydrogen generation, and reaction order based on (B) catalyst concentration, (D) $NaBH_4$ amount, (F) methanol content in PAP system. 264

Figure 5.14. (A) XRD profiles of neat NB, PAP, de-PAP as the spent catalyst and regenerated PAP, (B) Hydrogen release with regenerated PAP upto four additional cycles, and (C) Catalytic activity after regeneration cycles. 266
Figure 5.15. FESEM images of (A) PAP, (B) de-PAP, (C) re1-PAP, (D) re2-PAP, and (E) re3-PAP. 267
Figure 5.16. (A) FTIR spectra, (B) XRD profiles of PAP, re1-PAP, re2-PAP, and re3-PAP, Elemental distribution of (C) PAP, (D) re1-PAP, (E) re2-PAP, and (F) re3-PAP. 268

LIST OF TABLES

Chapter 1

Table 1.1. Chemical structures, synthesis conditions, and properties of polybenzoxazines and their carbon counterparts..... 29
Table 1.2. Textural properties of carbon structures subjected to carbonization and activation.... 56
Table 1.3. Electrochemical properties of polybenzoxazine-based carbon structures..... 63

Chapter 2

Table 2.1. Synthesis parameters for phloroglucinol, PEI, and formaldehyde-based polybenzoxazine particles. 95
Table 2.2. Textural characteristics of the polymer particles and the derived doped carbon structure..... 120
Table 2.3. Determination of elements present in the heteroatom-doped carbon obtained from as-synthesized polybenzoxazine..... 121

Chapter 3

Table 3.1. Textural properties of polybenzoxazine particles by N_2 adsorption isotherms at 77 K. 167
Table 3.2. Comparative dehydrogenation performance of different AB-polymer composites. . 185

Chapter 4

Table 4.1. Synthesis parameters for phloroglucinol, amines, and formaldehyde-based polybenzoxazine particles via template-free and templated strategies. 202
Table 4.2. Textural properties of polybenzoxazine particles by N_2 adsorption isotherms at 77 K. 215
Table 4.3. Textural properties of polybenzoxazine particle-derived heteroatom-doped carbon by N_2 adsorption-desorption isotherms at 77 K. 219

Table 4.4. Elemental distribution in the heteroatom-doped carbon systems derived from both 4-aminobenzonitrile and aniline-based polybenzoxazines..... 220

Chapter 5

Table 5.1. Synthesis parameters for phloroglucinol, 4-aminophthalonitrile, and formaldehyde-based polybenzoxazine particles..... 243

LIST OF ABBREVIATIONS

PBz	Polybenzoxazine
0D	Zero-Dimensional
RF	Resorcinol/Formaldehyde
DAH	1,6-Diaminohexane
^{13}C CP/MAS	^{13}C Cross-Polarization Magic-Angle Spinning
NMR	Nuclear Magnetic Resonance
1D	One-Dimensional
SEM	Scanning Electron Microscopy
FESEM	Field-Emission Scanning Electron Microscopy
PVB	Poly(vinylbutyral)
2D	Two-Dimensional
DMF	Dimethylformamide
THF	Tetrahydrofuran
PAN	Polyacrylonitrile
GO	Graphene oxide
Asn	Asparagine
Pluronic F127	Poly(ethylene oxide)$_{101}$-block-poly(propylene oxide)$_{56}$-block-poly(ethylene oxide)$_{101}$

SA	Stearic Acid
Span 85	Sorbitan Trioleate surfactant
Hypermer 1599	ABA-type polymeric ester surfactant
CTAB	Cetyltrimethylammonium bromide
TEOS	Tetraethyl orthosilicate
EDA	Ethylenediamine
AZD	Azodicarbonamide
CNT	Carbon nanotube
EISA	Evaporation-induced self-assembly
DMA	Dimethylamine
TMA	Trimethylamine
TEA	Triethylamine
TEPA	Tetraethylenepentamine
TEM	Transmission Electron Microscopy
Synperonic NP30	Nonylphenol ethoxylate
3D	Three-dimensional
TBOZ	Trifunctional Benzoxazine
PEM	Proton Exchange Membrane
SBA-15	Santa Barbara Amorphous-15 Mesoporous Silica

DFT	Density Functional Theory
HGR	Hydrogen Generation Rate
Py-GC/MS	Pyrolysis-Gas Chromatography-Mass Spectrometry

LIST OF SYMBOLS

C_{sp}	Specific Capacitance
I	Current
Δt	Discharge time
m	Weight of active material
ΔV	Operating potential window
C_a	Areal Capacitance
A	Projected area of electrode
E_d	Energy Density
P_d	Power Density
R_s	Series Resistance
R_{ct}	Charge-Transfer Resistance
E_a	Activation Energy